Journal of Fluids and Structures 114 (2022) 103751

Contents lists available at ScienceDirect

Journal of Fluids and Structures

journal homepage: www.elsevier.com/locate/jfs

On the feasibility of a flexible foil with passive heave to extract energy from low wind speeds

R. Fernandez-Feria *, E. Sanmiguel-Rojas

Fluid Mechanics Group, Universidad de Málaga, Dr Ortiz Ramos s/n, 29071 Málaga, Spain

ARTICLE INFO

Article history:
Received 14 May 2022
Received in revised form 25 July 2022
Accepted 29 August 2022
Available online 20 September 2022

Keywords:
Flexible oscillating foil
Flutter
Fluid–structure interaction
Wind turbine

ABSTRACT

We explore numerically and theoretically the capability of flexible foils elastically mounted to translational springs and dampers at the leading edge to extract energy from low-speed winds through its passive heave motion. Given the spring and foil stiffnesses, for each damper constant the theory (which is valid for high Reynolds numbers and small foil deflection amplitudes, i.e., in absence of separation) provides analytically a minimum wind velocity for flutter instability, above which energy can be harvested, that depends on the thickness-to-chord-length ratio of the foil. Simple analytical expressions for the flutter frequency are also provided. Minimum wind speeds and corresponding flutter frequencies are characterized for a carbon fiber foil as the spring stiffness and damper constant are varied, finding that energy can be extracted from wind speeds lower than in conventional wind turbines. These theoretical predictions are assessed from full numerical simulations at Reynolds numbers corresponding to these wind velocities and for chord lengths of the order of the meter (i.e. about 10^6) using appropriate turbulence models, which allow to compute the power extracted from the wind that the flutter stability analysis cannot provide.

1. Introduction

The search for new devices to extract energy from natural renewable resources has been motivated in the past few decades mostly by economic reasons, today reinforced by the urgency of mitigating climate change. Wind is already a very consolidated source of renewable energy, constituting a relevant fraction of the total electricity generation in many countries. Wind energy engineering remains an active field of research and innovation, mostly focussed on more efficient designs and configurations for the traditional rotating wind turbines (McKenna et al., 2022), and on the development of new and imaginative devices to extract energy from other configurations that may exploit more efficiently the wind–structure interaction (Tang et al., 2009; Hamlehdar et al., 2019; Lee et al., 2019).

It is in this last mentioned context that we analyze here, theoretically and computationally, the dynamics and performance of a flexible flapping-foil turbine concept which can extract energy from relatively low wind speeds (lower than 5 m/s, as we shall see). Research on hydrokinetic flapping-foil turbines that extract energy mechanically from the foils heaving and/or pitching motions has been very active in the past few years (see. e.g., the reviews by Xiao and Zhu, 2014; Young et al., 2014), specially using rigid flapping foils, in either fully constrained (Kinsey and Dumas, 2008; Zhu, 2012; Deng et al., 2014; Kim et al., 2017), semi-passive (Shimizu et al., 2008; Zhu et al., 2009; Zhu and Peng, 2009; Abiru and Yoshitake, 2011; Su and Breuer, 2019; Boudreau et al., 2019a,b) and fully passive (Peng and Zhu, 2009; Zhu,

* Corresponding author.
E-mail addresses: ramon.fernandez@uma.es (R. Fernandez-Feria), enrique.sanmiguel@uma.es (E. Sanmiguel-Rojas).

https://doi.org/10.1016/j.jfluidstructs.2022.103751

2012; Veilleux and Dumas, 2017; Wang et al., 2017; Boudreau et al., 2018, 2020) configurations. The energy harvesting performance of fully passive hydrofoils at the wake of different flow-induced vibration mechanisms has been recently assessed by Tamimi et al. (2022). However, rigid flapping foils using these purely mechanical devices are less effective for extracting energy from the usual wind velocities than from tidal and other natural water currents due to the much larger mass ratio of a foil in air than in water (McKinney and DeLaurier, 1981; Veilleux and Dumas, 2017). This difficulty can be mitigated with the use of flexible flapping foils elastically mounted to translational and torsional springs and dampers, whose flexural motion may resonate with either the heaving or the pitching passive motions, or with both coupled, in such a way that one may extract energy in a wider parametric range than with the rigid-foil counterpart (Fernandez-Feria, 2022). Particularly from much lower wind speeds, as it is shown in the present paper.

The power extraction efficiency of kinematically constrained hydrokinetic flapping-foil turbines has been shown to improve when some prescribed chordwise flexibility is added to the otherwise rigid foil motion (Liu et al., 2013; Quang and Hwan, 2015; Zhu et al., 2019), or when some parts of the foil are allowed to deform passively with the flow (Wu et al., 2015; Liu et al., 2016; Jeanmonod and Olivier, 2017; Liu et al., 2017). Fully-passive flexible flapping-foil hydrokinetic turbines have also been proposed based on piezoelectric or electromagnetic devices (Khaligh et al., 2010), commonly taking advantage of an external forcing such as the vortex shedding from a bluff body (Allen and Smits, 2001). But flutter instabilities in water currents, where the mass ratio is small, are only possible at high velocities (Shelley et al., 2005; Tang and Païdoussis, 2007; Eloy et al., 2008; Michelin et al., 2008), impeding energy harvesting from natural water currents when only a passive heaving motion is allowed, as shown in the present work. Spontaneous oscillations of the foil in natural water streams are only feasible when coupled pitch and heave passive motions are allowed to resonate jointly with the flexural motion of the flexible foil (Fernandez-Feria, 2022). In air, however, where the mass ratio is larger than in water, the foil may undergo flutter instabilities amenable to be used for wind-energy extraction with only passive heaving motion, and even for a clamped foil (Alben, 2008), but in the last case energy has to be extracted using piezoelectric devices (Tang et al., 2009). We show in the present study that just allowing for a passive heaving motion of the flexible foil suffices for energy extraction at particular resonant frequencies and low wind speeds. This relatively simple mechanical device is analyzed in what follows, both theoretically and numerically, for a two-dimensional (2D) flexible foil elastically mounted to a translational spring and a translational damper at the leading edge.

This configuration with just passive heave at the leading edge, i.e. without pitching nor selecting any other pivot axis, is chosen for its simplicity, both to facilitate the fully viscous numerical simulations of the flow interaction with the flexible-foil device and also from a manufacturing point of view. The theory shows that the most unstable flutter instabilities of a flexible plate are generated when the pivot point is close the leading edge, with no great differences when it is located upstream of the quarter chord point (Fernandez-Feria, 2022). On the other hand, as already mentioned, it is theoretically shown below that the device does not work in water without allowing for passive pitching. But, since it theoretically works in air without pitching, it is of interest to explore numerically the feasibility of this simpler device to extract energy from the wind, independently that it would perform better allowing for passive pitching, not necessarily at the leading edge. The study of the effect of passive pitching combined with the pivot axis location is left for a future, more demanding numerical work.

2. Results from the flutter instability analysis

We consider first the linear flutter instability of a two-dimensional (2D) flexible foil of chord length c, constant thickness ε, density ρ_s, and elastic modulus E, elastically mounted to a translational spring of constant $\tilde{k}_h$ and a damper of constant $\tilde{b}_h$ at the leading edge, but with the pitching or rotational motion mechanically inhibited at this point (see Fig. 1, where the dimensionless quantities defined just below are used; note that dimensional quantities are written with a tilde $\tilde{}$ whenever the same symbol is used below for its dimensionless counterpart). When subjected to a uniform air current with velocity U, this mechanical system may become unstable if U exceeds a critical velocity U^* which depends on all the above parameters, triggering a coupled heaving and flexural motion of the foil. To analyze this instability, we consider the linearized dynamical equations taking into account the forces exerted by the fluid on the foil in the inviscid limit.

Dimensionless variables and parameters are used, scaling all magnitudes with $c/2$, U, and the air density ρ as characteristic length, velocity and mass, respectively. The equations for the non-dimensional heaving, $h(t)$, and chordwise flexural, $d(t)$, motions are the following [see Fernandez-Feria (2022) for the present case with no pitching motion, the pivot point located at the leading edge, $a = -1$, and the centre of mass at the centre of the foil, $x_0 = 0$; the dots denote differentiation with respect to the dimensionless time t, which is scaled with $c/(2U)$]:

$$m\ddot{h} + J_a\ddot{d} = C_L - k_h h - b_h\dot{h}\,, \tag{1}$$

$$I_a\ddot{h} + K_d\ddot{d} + \frac{16}{9}\,S\,d = C_F\,. \tag{2}$$

These equations are obtained by integrating between $x = -1$ and $x = 1$ the Euler–Bernoulli beam equation and that equation multiplied by $(x + 1)$, respectively, assuming that the foil centerline $z_s(x, t)$ can be approximated by a quartic

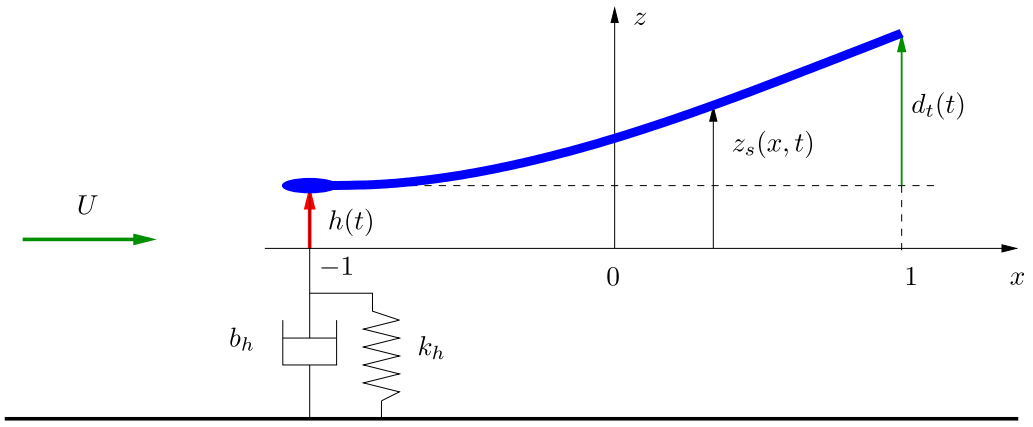

Fig. 1. Schematic of the flexible heaving foil (all quantities are dimensionless, except for the velocity U).

polynomial of the form (Fernandez-Feria and Alaminos-Quesada, 2021)

$$z_s(x,t) = h(t) + (x+1)^2 d(t) - (x+1)^3 \frac{d(t)}{3} + (x+1)^4 \frac{d(t)}{24}\,, \quad -1 \le x \le 1\,, \tag{3}$$

when the non-dimensional heave and flexural deformation are both small, i.e., assuming $|h| \ll 1$ and $|d| \ll 1$. This expression satisfies $z_s = h(t)$ and $\partial z_s/\partial x = 0$ at $x = -1$ (passive heave with no pitching at the leading edge) and $\partial^2 z_s/\partial x^2 = \partial^3 z_s/\partial x^3 = 0$ at $x = 1$ (free trailing edge). The flexural deflection at the trailing edge relative to an otherwise identical rigid foil with the same heaving motion is then $d_t(t) = 2d(t)$.

In Eqs. (1)–(2), C_L and C_F are the lift and flexural coefficients, respectively, related to the pressure that the fluid exerts on the foil by

$$C_L(t) = \int_{-1}^{1} \Delta C_p(x,t)dx\,, \quad C_F = \int_{-1}^{1} (x+1)^2 \Delta C_p(x,t)dx\,, \tag{4}$$

where $\Delta C_p(x,t) = (p^- - p^+)/(\rho U^2)$ is the non-dimensional pressure difference between the lower (superscript $^-$) and upper (superscript $^+$) sides of the foil. The non-dimensional stiffness S and mass ratio m of the foil are defined as

$$S = \frac{E\varepsilon^3}{\rho U^2 c^3}\,, \quad m = 4\frac{\rho_s \varepsilon}{\rho c}\,. \tag{5}$$

The moment of inertia I_a and the coefficients J_a and K_d are, in this case of a uniform foil pivoting at the leading edge,

$$I_a = \frac{4}{3}m\,, \quad J_a = \frac{4}{5}m\,, \quad K_d = \frac{568}{315}m\,. \tag{6}$$

Finally, the non-dimensional spring stiffness k_h and the non-dimensional constant of the linear damper b_h are related to their dimensional counterparts through

$$k_h = \frac{\tilde{k}_h}{\rho U^2}\,, \quad b_h = \frac{2\tilde{b}_h}{\rho U c}\,. \tag{7}$$

For a rigid foil ($S \to \infty$ and, consequently, $d = 0$), Eq. (2) and the coefficients in (6) are not needed.

Following Fernandez-Feria (2022), to analyze the flutter stability of the system we consider small, harmonic perturbations of the form

$$h(t) = \mathrm{Re}\left[H_0 e^{i\gamma t}\right]\,, \quad d(t) = \mathrm{Re}\left[D_0 e^{i\gamma t}\right]\,, \tag{8}$$

where Re means real part and γ, H_0, and D_0 are in general complex quantities, with $|H_0| \ll 1$, $|D_0| \ll 1$, and

$$\gamma \equiv k + i\sigma\,, \quad k = \frac{\omega c}{2U} = \frac{\pi f c}{U}\,. \tag{9}$$

k is the non-dimensional, or reduced, frequency, being ω the dimensional frequency of the perturbations (f is the frequency in Hz), and $-\sigma$ their non-dimensional growth rate. For this harmonic motion the force coefficients (4) can be expressed in a closed analytical form, so that Eqs. (1)–(2) are transformed into a linear system of two algebraic, complex equations for H_0 and D_0:

$$\mathbf{A}(\gamma)\cdot\mathbf{X} = \mathbf{0} \quad \text{with} \quad \mathbf{A} = \begin{pmatrix} A_{11} & A_{12} \\ A_{21} & A_{22} \end{pmatrix}\,, \quad \mathbf{X} = \begin{pmatrix} H_0 \\ D_0 \end{pmatrix}\,, \tag{10}$$

where the different coefficients A_{ij} are given in Appendix.

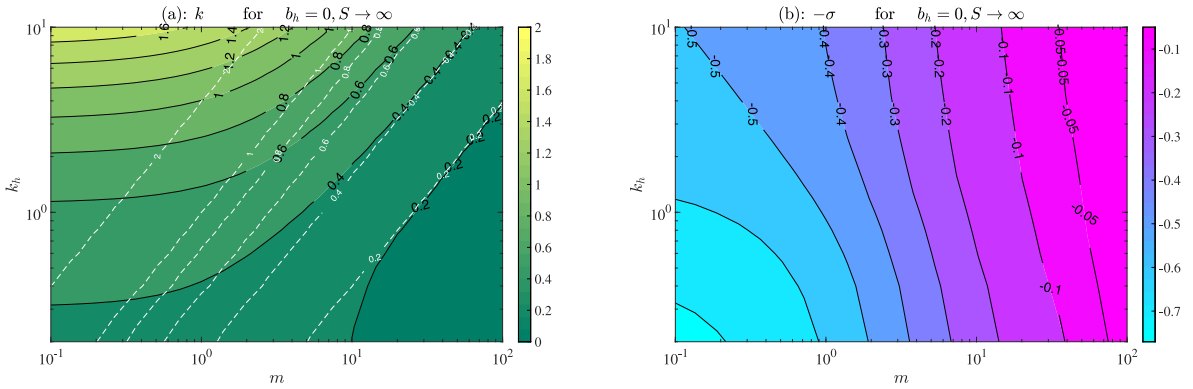

Fig. 2. Contours of k (a) and $-\sigma$ (b) in the $m - k_h$ plane for $b_\alpha = 0$ and $S \to \infty$. Dashed contours in (a) correspond to the resonant frequency in vacuum (13).

For a given set of values of the different non-dimensional parameters, namely, m, S, k_h and b_h, the system has nontrivial solutions for specific values of γ satisfying

$$\det[\mathbf{A}(\gamma)] = 0\,, \tag{11}$$

algebraic equation that fixes the oscillations frequency k if the system is unstable, i.e., if $\sigma < 0$. For $\sigma > 0$, any small perturbation in z_s will be damped. Thus, of particular relevance for the energy harvesting problem is the characterization of the parameters for neutral stability, i.e., for $\sigma = 0$, and the corresponding *natural* frequencies, $k = k_n$ say. Within the region of the parameter space where $\sigma < 0$, a passive heave motion of the foil is allowed according to the linear theory, which may be used to extract energy from the current. This region and the corresponding frequencies will be explored below for air winds of different velocities on foils with different thickness-to-chord ratios ε/c, and elastically supported to springs and dampers of different rigidities. As shown in Fernandez-Feria (2022), the present linearized approximation is accurate provided that the foil stiffness is not small, i.e. for $S \gtrsim 1$.

Eq. (11) for the complex eigenvalue γ is solved numerically using the Matlab function *fsolve*, starting from the leading neutral frequency corresponding to a rigid foil ($D_0 = 0$) when the fluid–structure interaction (FSI) is neglected. In this case, the equation simplifies to

$$-m\gamma^2 + ib_h\gamma + k_h = 0\,. \tag{12}$$

The imaginary part of the solution to this equation is never negative, so that the system with a rigid foil in vacuum is never unstable. It is neutrally stable ($\sigma = 0$) in the absence of damper ($b_h = 0$), with a natural frequency corresponding to the (non-dimensional) resonant frequency of a plate attached to a translational spring in vacuum:

$$k_n = k_{r0} = \pm\sqrt{\frac{k_h}{m}}\,. \tag{13}$$

If the FSI is taken into account, the rigid foil remains stable for all values of the remaining parameters, which means that no flutter instabilities are possible for a rigid foil with just heaving motion. One has to allow for a passive pitching motion (in this case about the leading edge) to be able to extract energy from a current with a rigid two dimensional foil (Fernandez-Feria, 2022). This is illustrated in Fig. 2, where the frequency k and the growth rate $-\sigma$ are plotted in the $m - k_h$ plane for $S \to \infty$ when $b_h = 0$ (remember that the system becomes more stable as the damper constant b_h increases). We observe that $\sigma > 0$ for all cases, while the corresponding frequency $k \to k_{r0}$ as $m \to \infty$, when the FSI becomes negligible. Note in Fig. 2 that $k \simeq k_{r0}$ for sufficiently high values of m when k_h is also large enough. Otherwise, the FSI effect on the natural frequency is very relevant.

Instabilities for a heaving-only foil become possible for a flexible foil, i.e., for finite S. In fact, as the foil stiffness S decreases for a given value of k_h, flutter instability may appear only for sufficiently large mass ratio m and for sufficiently small damper constant b_h, as shown in Fig. 3 for $k_h = 1$. The neutral curve of instability, $S = S^*(k_h, b_h, M) > 1$, appears in this case for $m > m^*(k_h, b_h) \simeq 3$ when $b_h = 0$, and for $b_h < b_h^*(k_h, m) \simeq 2.75$ for $m = 10$. This map of the unstable regions as the stiffness S decreases is qualitatively very similar in a wide range of values of the spring constant k_h. The corresponding frequencies comes also from the complex Eq. (11). An approximation can be obtained neglecting the FSI and assuming b_h is small compared with both m and k_h (for $b_h = 0$ the system is neutrally stable, so that the following values of k are in fact neutral or natural frequencies):

$$k_n \simeq k_{r0d} = \sqrt{\frac{70}{58}\frac{S}{m}}\sqrt{1 + \frac{71}{70}\frac{k_h}{S} + \sqrt{1 + \frac{13}{35}\frac{k_h}{S} + \frac{5041}{4900}\left(\frac{k_h}{S}\right)^2}}\,. \tag{14}$$

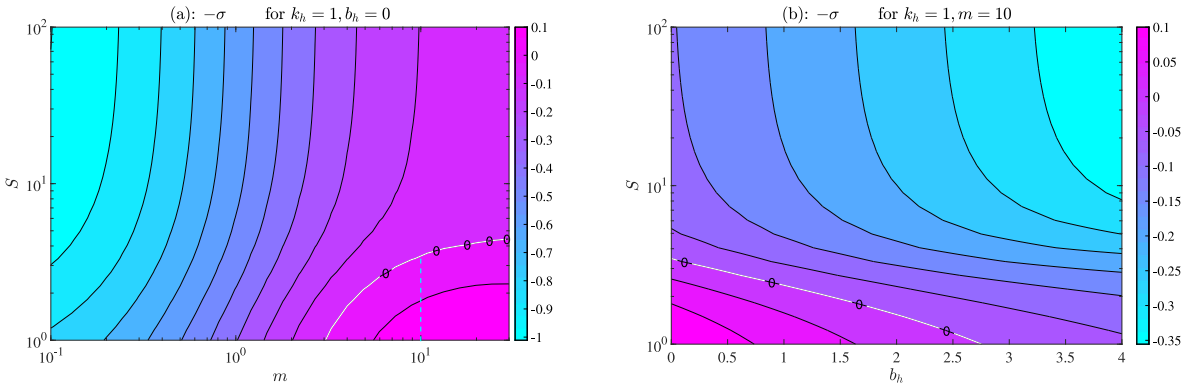

Fig. 3. Contours of the growth rate $(-\sigma)$ for $k_h = 1$ in the $m - S$ plane for $b_h = 0$ (a), and in the $b_h - S$ plane for $m = 10$ (b). The neutral curves are labeled with '0'. Marked in (a) is the unstable segment for $m = 10$, from which starts the neutral curve in (b) at $b_h = 0$.

For $k_h/S = (\tilde{k}_h/E)(c/\varepsilon)^3 \ll 1$, which is a physically relevant limit owing to the fact that S is usually large, one has, in first approximation,

$$k_{r0d} \simeq \sqrt{\frac{70}{29}\frac{S}{m}}\,. \tag{15}$$

In dimensional form, this frequency (14) [or (15)] is independent of the velocity, and proportional to ε/c^2. In Hz, for $k_h/S \ll 1$,

$$f_{r0d} \simeq \sqrt{\frac{35}{58}\frac{E}{\rho_s}}\,\frac{\varepsilon}{\pi c^2}\,. \tag{16}$$

Since m has to be larger than unity, these instabilities cannot occur in water currents when $S > 1$ because the values of the mass ratio m are much smaller than unity for thin foils and usual values of the material density ρ_s. Thus, a heaving-only flexible foil cannot be used as a hydrokinetic turbine, and that is why we consider here only the case of air currents, or wind turbines. In air, m may range between order unity and order one hundred, depending on the relative thickness ε/c and the foil material (see below). On the other hand, the value of the damper constant b_h has to be sufficiently small to allow for flutter instabilities, but not so small to be negligible the energy harvested from the wind by the device (see Section 4 below for the computation of the power output from the numerical simulations.)

The condition $S < S^*(k_h, b_h, m)$ for flutter instability yields a minimum velocity above which the system may extract energy from the wind for a given foil material as a function of the relative thickness:

$$U > U^* = \left(\frac{E}{\rho S^*}\right)^{1/2}\left(\frac{\varepsilon}{c}\right)^{3/2}, \quad m = \frac{4\rho_s}{\rho}\frac{\varepsilon}{c} > m^*\,. \tag{17}$$

Since S^* is an order-of-unity function, Eq. (17) provides a useful guide to select elastic modulus and thickness-to-chord ratio for reducing the critical wind flutter velocity, while Eq. (16) provides an approximation for the flutter frequency for a given chord length and foil density.

Because the mass ratio m depends only on ε/c for a given material in air, U^*, and therefore the instability region, only depends on the spring and damper constants (through the function S^*) once the foil material is selected. Fig. 4 shows these regions in the $\varepsilon/c - U$ plane through the corresponding neutral curves for carbon fiber (CF) ($E = 75 \times 10^9$ N/m^2, $\rho_s = 1\,400$ kg/m^3) in air ($\rho = 1.225$ kg/m^3) for $\tilde{b}_h = 0$ and 1 kg/m s (per unit span and using $c = 1$ m) and increasing values of $\tilde{k}_h$. Also shown is the curve corresponding to $S = 1$, above which $S < 1$ and the results of the present analysis are not longer valid. We have selected this material as an example because its well known excellent mechanical properties and relative low density and large fatigue life compared, for instance, with metals such as aluminum or steel.

From Fig. 4 it is clear that the minimum velocity for instability increases with the damper constant $\tilde{b}_h$, and that, for a given $\tilde{b}_h$, there is a value of the spring constant which provides the lowest U^* within the validity range $S \gtrsim 1$. In the cases plotted in Fig. 4 this happens for $\tilde{k}_h \approx 100$ when $\tilde{b}_h = 0$, and for $\tilde{k}_h \approx 75$ when $\tilde{b}_h = 1$ (all dimensional quantities are in SI units), being the corresponding lowest flutter velocities about 4.5 m/s and 6 m/s, respectively. The contours of the growth rate $(-\sigma)$ and the corresponding frequencies in Hz ($f = Uk/\pi c$, with $c = 1$ m) for these two cases are depicted in Figs. 5 and 6. The circles in these two figures correspond to the cases where the numerical simulations described in the following sections are performed.

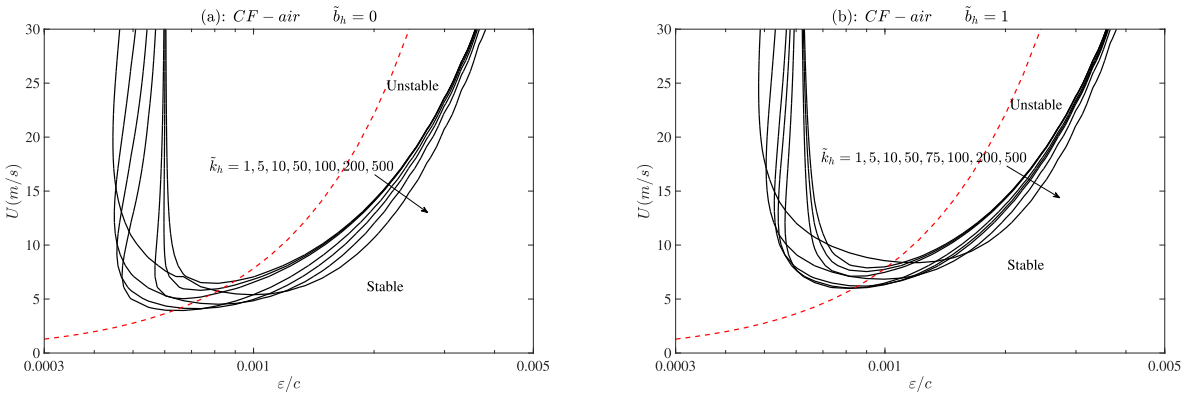

Fig. 4. Neutral curves for flutter instability in the $\varepsilon/c-U$ plane for a carbon fiber foil in air for increasing values of the spring constant $\tilde{k}_h$ and two values of the damper constant, $\tilde{b}_h=0$ (no damper) (a) and $\tilde{b}_h=1$ (b) (all dimensional quantities are in SI units; the results for $\tilde{b}_h$ are computed using $c=1$ m). The dashed curves correspond to $S=1$, and only below them the present linear stability results are valid.

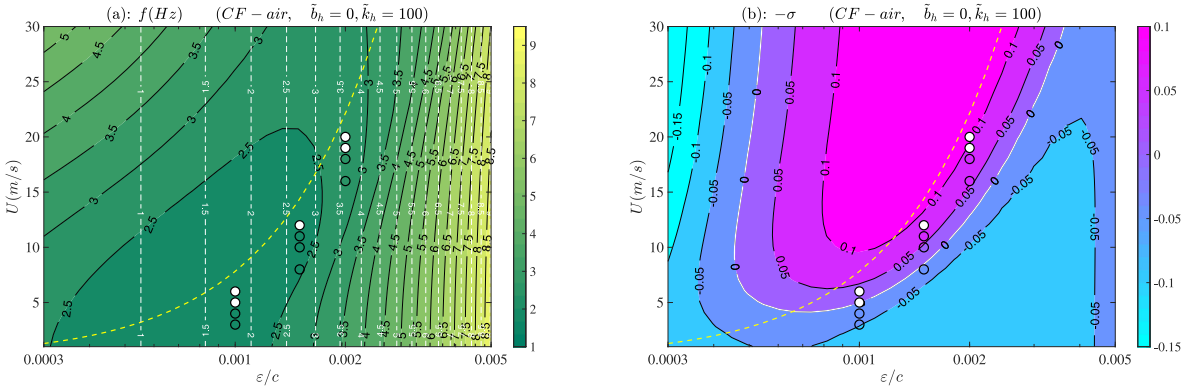

Fig. 5. Contours of f (a) and $-\sigma$ (b) in the $\varepsilon/c-U$ plane for a carbon fiber foil in air with $\tilde{b}_h=0$, $c=1$ m and $\tilde{k}_h=100$ kg/m s^2. Neutral curve marked with '0' in (b). Dashed curves correspond to $S=1$ and dashed contour lines in (a) to the resonant frequency in vacuum (16). Circles correspond to the numerical simulations (see Section 4).

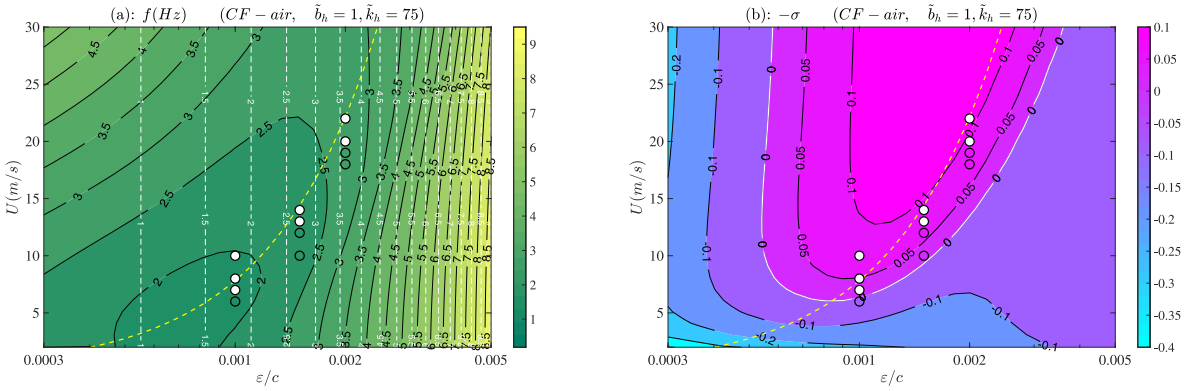

Fig. 6. As in Fig. 5, but for $\tilde{b}_h=1$ kg/m s and $\tilde{k}_h=75$ kg/m s^2.

3. Numerical simulation: Formulation and computational method

For the numerical simulations we consider air flow over a 2D carbon fiber plate embedded in a head consisting of a NACA0015 profile, which acts as the leading edge (LE) of the foil. The total chord length of the foil (head + plate) is $c=1$ m, of which the NACA0015 at the LE occupies a length of $c/20$ [see Fig. 7(b) for a sketch not to scale, together with the computational domain described below, and also Figs. 8 and 10 for actual pictures of the foil]. Computations are

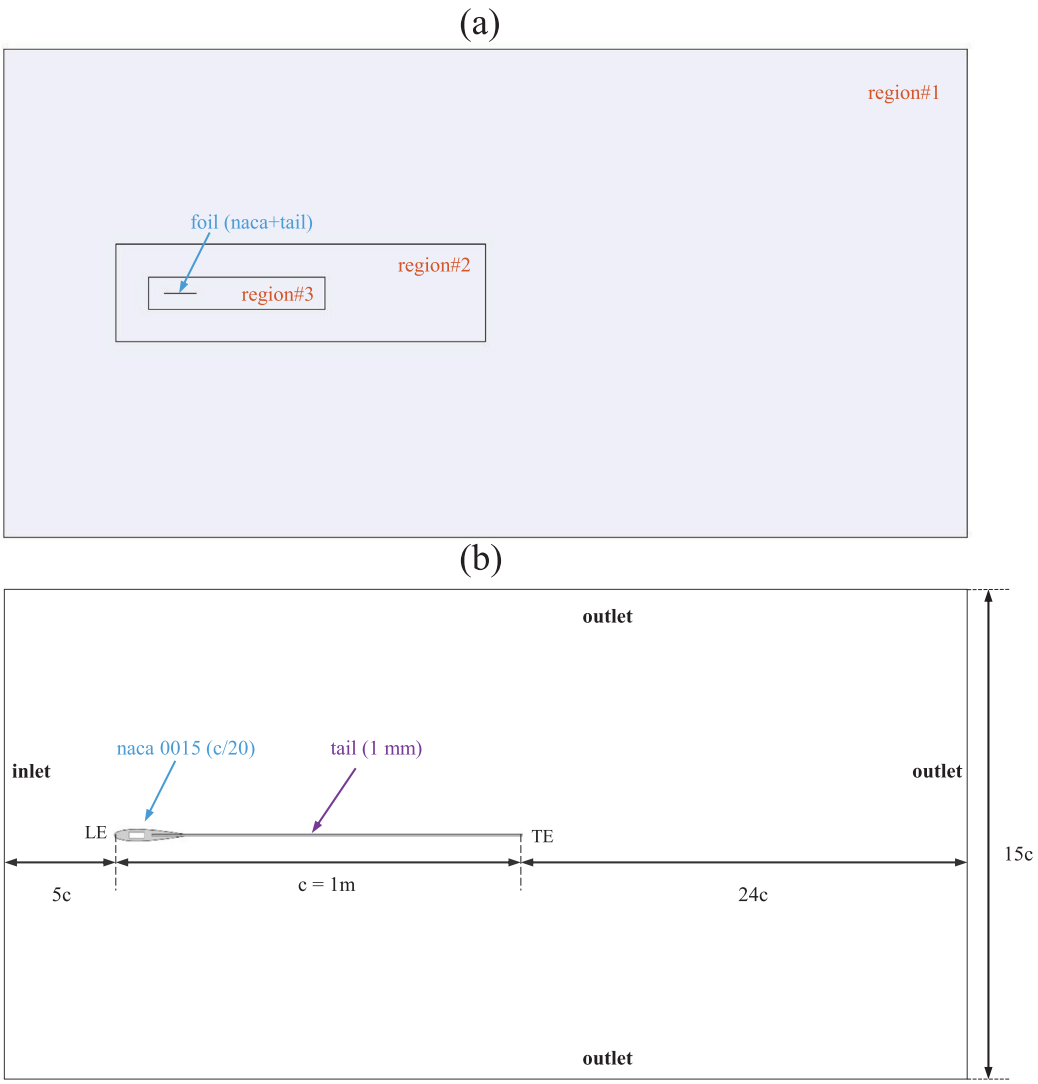

Fig. 7. (a) Computational domain and subdomains (to scale). (b) Different dimensions of the foil and the computational domain (not to scale).

performed with plate thicknesses $\varepsilon = 1$, 1.5 and 2 mm. Thus, the thickness-to-chord ratio in the numerical simulations are $\varepsilon/c = 10^{-3}$, 1.5×10^{-3} and $\varepsilon/c = 2 \times 10^{-3}$. The density of the NACA0015 head is selected in each case for the foil centre of mass to be always located at its middle point, like in the theoretical results reported in Figs. 4–6, and the non-dimensional mass ratios are $m \simeq 4.57$, 6.86 and 9.14, respectively

To solve numerically the coupled FSI problem we use the finite volume-based solver Ansys-Fluent v21.2. Specifically, since the Reynolds number is about 10^6, the flow is solved using the $k-\omega$ SST turbulence model, well suited to resolve transitional and developed turbulent flows at these Reynolds numbers. Although turbulence is inherently three-dimensional, we consider that the mean flow is 2D, so that in the third direction turbulence is assumed to be homogeneous (i.e., statistically invariant under translations of the reference frame). In these cases, if one uses a RANS approach, like the $k-\omega$ SST turbulence model employed in the present work, one may solve for the mean flow variables using 2D equations. This kind of 2D RANS turbulence modeling, particularly with the $k-\omega$ SST turbulence model implemented in the solver package ANSYS Fluent, has been sufficiently validated experimentally for similar aerodynamic problems (e.g., Gharali and Johnson, 2013). On the other hand, the intrinsic FSI algorithm is used to simulate the fluid–structure coupling. Both approaches are described in detail, and validated with experimental data, in recent publications by the authors (Sanmiguel-Rojas and Fernandez-Feria, 2021, 2022). In particular, a comparison with experimental data by Heathcote and Gursul (2007) for a similar heaving flexible foil is made in Figs. 4 and 5 of Sanmiguel-Rojas and Fernandez-Feria (2021). Transient, pressure-based, coupled solver with absolute velocity formulation are the settings for solution of all simulations. The least-squares cell based method is applied for calculating the gradients of the transport

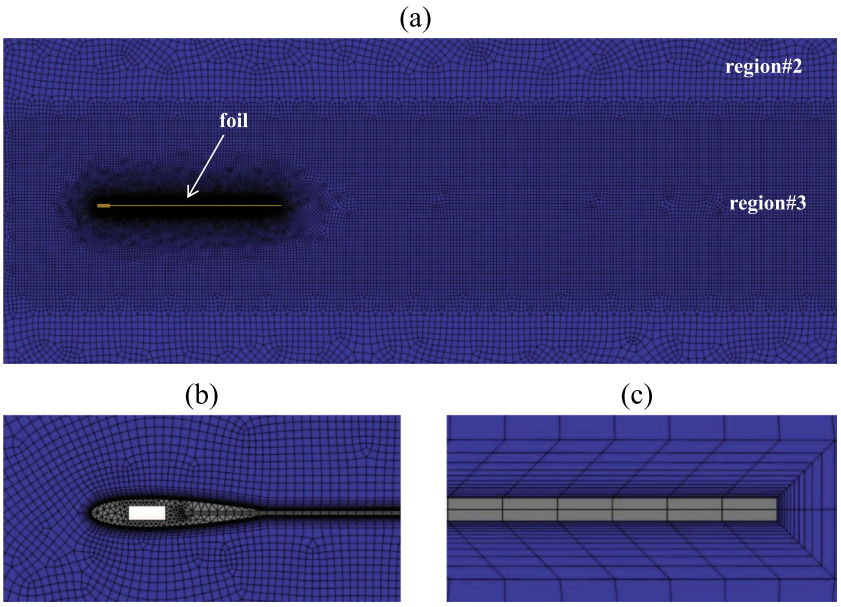

Fig. 8. Different views of mesh#1 for $\varepsilon/c = 10^{-3}$.

quantities on the faces of the cells. The spatial discretization methods in all FSI simulations are solved with second order for the pressure term, and second-order upwind for continuity and momentum equations. The explicit relaxation factors of pressure and momentum are set at 0.75 to ensure the stability of the numerical method. First order implicit formulation is applied for discretizing the flow time derivatives, ensuring stability for transient structures using the method by Newmark (1959), setting the amplitude decay factor to $\gamma = 0.1$ to get full stable solutions. At each time step, convergence is considered that has been reached once the absolute residuals values 10^{-3}, 10^{-3}, 10^{-5} and 10^{-7} are fulfilled for continuity, turbulence, momentum and structure quantities, respectively. All simulations start from rest. To smooth the mesh in the dynamic-mesh method we used the boundary distance diffusion method, with a diffusion parameter set to 1.75. The algebraic multi grid (AMG) with the conjugate gradient (CG) for pre-conditioning is used for stabilizing the dynamic mesh.

Fig. 7(a) shows the computational domain (width $= 15c \times$ length $= 30c$) used in all the simulations, including to scale the different regions into which the computational domain is decomposed to ease the meshing procedure described below. With larger computational domains the results remained practically unchanged, even for the most computationally demanding cases. Fig. 7(b) displays a schematic not to scale with the dimensions used in the computations, together with an indication of the boundary conditions. These are: a uniform velocity profile at the inlet, located at a distance $5c$ upstream of the foil LE; non-slip wall condition on the foil, and pressure outlet $p = 0$ on the rest of the boundaries. Inside the head of the foil a support is included [see rectangular hole inside the NACA0015 in Fig. 8(b)], which is necessary to emulate the effect of the forces exerted by the spring and damper at the foil LE. These forces are emulated by a User Defined Function (UDF), i.e., a *C* program compiled in Fluent.

A mesh convergence study was performed by doubling the number of cells with the following three meshes: mesh#0 (coarse) with 60 956 cells, 588 cells on the profile and a time step $\Delta\tilde{t} = 2 \times 10^{-4}$ seconds; mesh#1 (medium) with 109 912 cells, 832 cells on the profile and a time step $\Delta\tilde{t} = 10^{-4}$ seconds; mesh#2 (fine) with 209 824 cells, 1 176 cells on the profile and a time step $\Delta\tilde{t} = 0.5 \times 10^{-4}$ seconds. Two cells are placed in the thickness of the plate for the three meshes [see Fig. 8(c)]. The time step was set to guarantee a maximum $CFL < 5$ in all cases to avoid numerical instabilities due to the FSI coupling. The meshes of the fluid region include only quad elements with a maximum skewness < 0.52. In order to capture correctly the boundary layer around the foil, we set an inflation layer of 12 cells with a growth rate 1.2 and the first cell thickness of size 0.1, 0.071 and 0.05 mm for the meshes #0, #1 and #2, respectively [see Figs. 8(b) and (c)]. This first layer thickness guarantees a maximum $y^+ < 1$ on the foil wall, even for the cases with the highest inlet velocity reported here, i.e., $U = 15$ m/s (Reynolds number based on the chord length $Re = Uc/\nu \simeq 1.027 \times 10^6$, where ν is air's kinematic viscosity). Fig. 8 depicts different views of the mesh#1 for $\varepsilon/c = 10^{-3}$.

The results of the mesh convergence analysis are displayed in Fig. 9 in terms of the time evolution of the dimensionless trailing edge position z_t (scaled with $c/2$), and the lift coefficient, C_L, both computed with the three meshes for one of the most unfavorable cases analyzed, i.e., $\tilde{k}_h = 75$ kg/ms^2, $\tilde{b}_h = 1$ kg/ms, $\varepsilon/c = 10^{-3}$ and $U = 15$ m/s. The lift coefficient is defined as

$$C_L = \frac{F_z}{\rho U^2 c/2}\,, \tag{18}$$

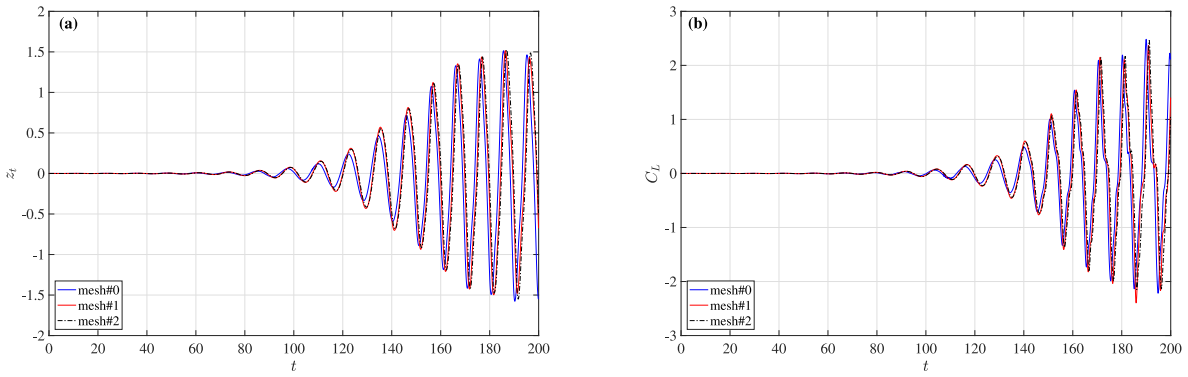

Fig. 9. Mesh convergence study in terms of the time evolution of the dimensionless trailing edge position (a) and the lift coefficient (b), computed with the three meshes for $\tilde{k}_h = 75$ kg/ms^2, $\tilde{b}_h = 1$ kg/ms, $\varepsilon/c = 10^{-3}$, and $U = 15$ m/s.

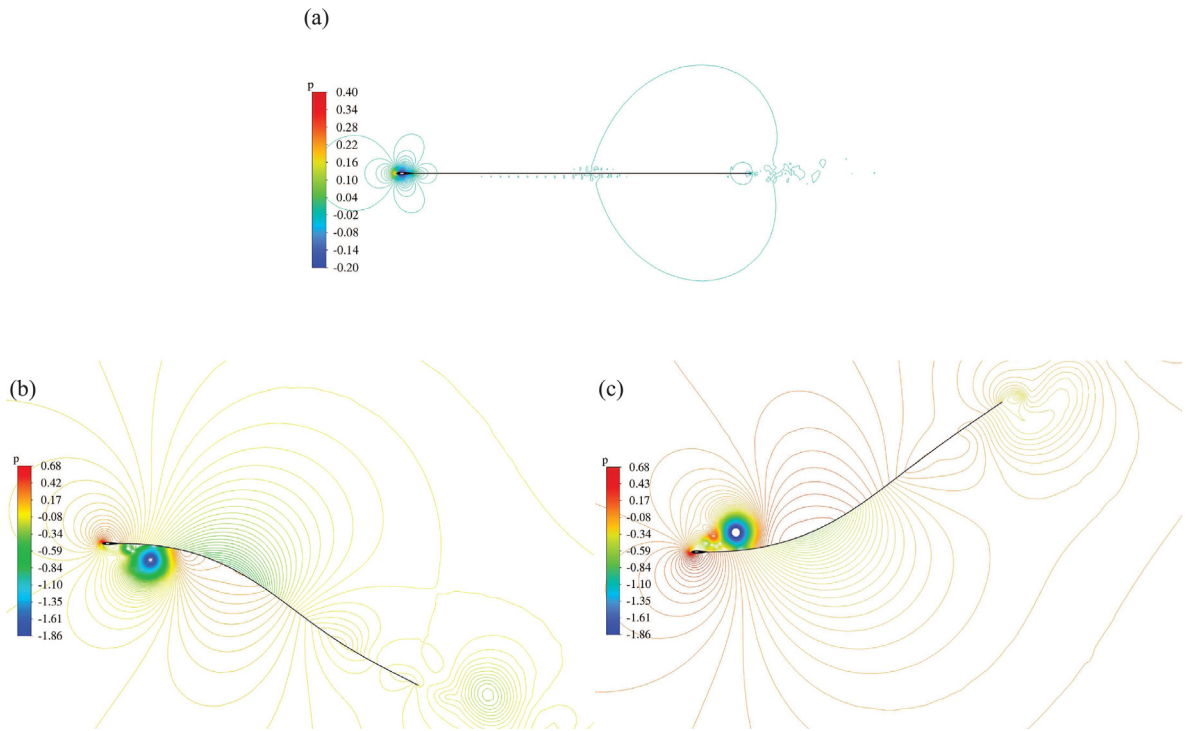

Fig. 10. Snapshots of dimensionless pressure contours when $\tilde{k}_h = 75$ kg/ms^2, $\tilde{b}_h = 1$ kg/ms, $\varepsilon/c = 10^{-3}$ for a stable case with $U = 5$ m/s (a), and for an unstable case with $U = 15$ m/s at two instants within a cycle, at the beginning (b) and at mid cycle (c).

where F_z is the $z-$component of the total force (per unit span) exerted by the fluid on the foil. It is observed in Fig. 9 that the differences between the results obtained with meshes #1 and #2 are negligible, indicating that both are very close to mesh independence. Consequently, we select the medium mesh#1 for all the numerical results reported below.

4. Numerical simulation: Results

The results plotted in Fig. 9 clearly shows an unstable case: small (numerical) perturbations eventually grow exponentially and saturate. Thus, the flutter instability of the foil reaches a final oscillatory self-sustained state of relatively large amplitude which, in Fig. 9, is characterized by the oscillation of the trailing edge position and the consequent oscillatory force that the fluid exerts on the foil due to its passive heaving and flexural motions. The case considered in Fig. 9 corresponds to an unstable case in Fig. 6, well above the neutral curve in Fig. 6(b). A visualization of the final oscillatory flow for this case is depicted in Figs. 10(b) y (c) in terms of the non-dimensional pressure field at two instants of time within a cycle, at the beginning, when the LE is located at $z = 0$ and the foil is going up [Fig. 10(b)], and in the

middle of the cycle, when the LE is also at $z = 0$ but the foil is going down [Fig. 10(c)]. On the other hand, Fig. 10(a) shows the non-dimensional pressure field for a stable case corresponding to the same structural conditions but for a wind velocity $U = 5$ m/s. The flow and the foil remain steady in this case, which lies below the neutral curve in Fig. 6(b) (neither of the two cases considered in Fig. 10 is marked in Fig. 6; see below for all the cases marked in Figs. 5 and 6 corresponding to different numerical simulations).

As discussed above, the permanent oscillatory state of the plate, triggered by the flutter instability above a critical wind velocity U^* (for given ε/c and the mechanical properties of the foil, spring and damper), may be used to extract energy from the wind. Assuming that all the loss of mechanical energy in the linear damper is converted into electric energy, as was done in previous works that considered a passive heave motion (e.g., Abiru and Yoshitake, 2011; Wang et al., 2017; Boudreau et al., 2020), the non-dimensional power output (per unit span) can be written as [it is the last term in Eq. (1) multiplied by $-\dot{h}$, corresponding to the power output per unit span scaled with $\rho U^3 c/2$]:

$$C_P = \frac{\tilde{b}_h(\dot{\tilde{h}})^2}{\frac{1}{2}\rho U^3 c} = b_h \dot{h}^2 \,. \tag{19}$$

Of special relevance is its time average over a cycle of the oscillations (the non-dimensional period is $T = 2\pi/k$),

$$\overline{C}_P = \frac{k}{2\pi}\int_t^{t+2\pi/k} C_P(t)dt \,, \tag{20}$$

and the energy efficiency, defined as the fraction of the incoming wind kinematic energy flux per unit span, $\rho U^3 \Delta\tilde{z}_t/2$, recovered by the system (Xiao and Zhu, 2014; Young et al., 2014),

$$\eta = \frac{2\overline{C}_P}{\Delta z_t} \,, \tag{21}$$

where $\Delta z_t = 2\Delta\tilde{z}_t/c$ is the maximum of the non-dimensional distance swept by the trailing edge. Actually, to compute the time-average power coefficient $\overline{C}_P$ once the final oscillatory state has been reached we use the last four cycles.

We have performed a series of numerical simulations for the conditions marked with circles in Figs. 5 and 6, white filled if the system becomes unstable and with open circles for the stable cases. They correspond to the two couples of values of $\tilde{b}_h$ and $\tilde{k}_h$ selected in Section 2 for a CF plate with $c = 1$ m in air, and three thickness-to-chord ratios, $\varepsilon/c = 10^{-3}$, 1.5×10^{-3} and 2×10^{-3}. For each one of these thicknesses the wind velocity U has been increased from a low value where the system remains stable, up to a higher value of U above the flutter instability threshold. The resulting dimensionless time evolutions of the leading- and trailing-edge positions, $h(t)$ and $z_t(t)$, are reported in Figs. 11 and 12 for a total of 24 numerical simulations. All the numerical simulations are made until a final permanent state has been reached, many of them demanding more than a week of CPU in a supercomputer. But only an initial interval of each computation is shown in Figs. 11 and 12 to capture the flutter instability, if any.

We observe, for instance, that for $\tilde{k}_h = 100$ kg/ms^2 and $\tilde{b}_h = 0$ with $\varepsilon/c = 10^{-3}$ [Fig. 11(a)] the system is stable for $U = 3$ and 4 m/s, while it clearly becomes unstable for 5 and 6 m/s. Therefore, the threshold wind velocity for flutter instability is between 4 and 5 m/s for this thickness of the foil, which is in close agreement with the theoretical results shown in Fig. 5(b) for $\varepsilon/c = 10^{-3}$ (remember that unstable cases are marked with white-filled circles). Similarly, for the same $\varepsilon/c = 10^{-3}$ but for $\tilde{k}_h = 75$ kg/m s^2 and $\tilde{b}_h = 1$ kg/m s [Fig. 12(a)], the threshold wind velocity for flutter instability found with the numerical simulations lies between 6 and 7 m/s, also in close agreement with the theoretical prediction in Fig. 6(b) for $\varepsilon/c = 10^{-3}$. However, as the thickness of the plate increases, and so does the wind velocity for flutter instability [see Eq. (17)], the numerical results for the critical flutter velocity are larger than the theoretical predictions, as can be seen with the white-filled circles in Figs. 5(b) and 6(b) for the larger thicknesses $\varepsilon/c = 1.5 \times 10^{-3}$ and 2×10^{-3}.

This discrepancy can be explained by the fact that for these larger flutter velocities the flow separates on the extrados of the plate, the more so the larger the resulting heaving velocity $\dot{h}$ and the deflection of the plate, so that the predictions of the potential theory fail. However, at the much smaller critical flutter velocities for the thinnest plate, the flow remains mostly attached on both sides of the plate and the predictions of the inviscid theory are more accurate. This behavior can be observed in Fig. 13, where a comparison is made between the instantaneous flow fields around two plates with different relative thicknesses, $\epsilon/c = 10^{-3}$ and $\epsilon/c = 2 \times 10^{-3}$, for wind velocities just above the corresponding critical flutter velocities found numerically in Fig. 12; i.e. $U = 8$ m/s and $U = 20$ m/s, respectively. The figure shows snapshots of the dimensionless turbulent kinetic energy at the beginning of a cycle in the permanent oscillatory motion reached after the flutter instability, when the leading edge is at $z = 0$ and going up with the maximum heaving velocity. Clearly, the flow in the case with $U = 8$ m/s remains practically attached on both sides of the plate, except for a small leading edge vortex developing on the intrados of the plate, while in the case with $U = 20$ m/s the flow is fully separated on the extrados. This separation is a consequence not only of the larger wind velocity, that hinder the bending of the flow over the deflected plate, but also of the larger heaving velocity resulting from the flutter instability, which increases the effective angle of attack at the leading edge. Actually, the maximum non-dimensional flutter velocity, $\dot{h}_{max}$, occurring at the instant when $h(t) = 0$, is the tangent of the maximum effective angle of attack at the leading edge. For the cases plotted in Fig. 13, they are $\dot{h}_{max} = 0.4$ and 0.44, respectively, corresponding to angles of attack 21° and 24°. The values of

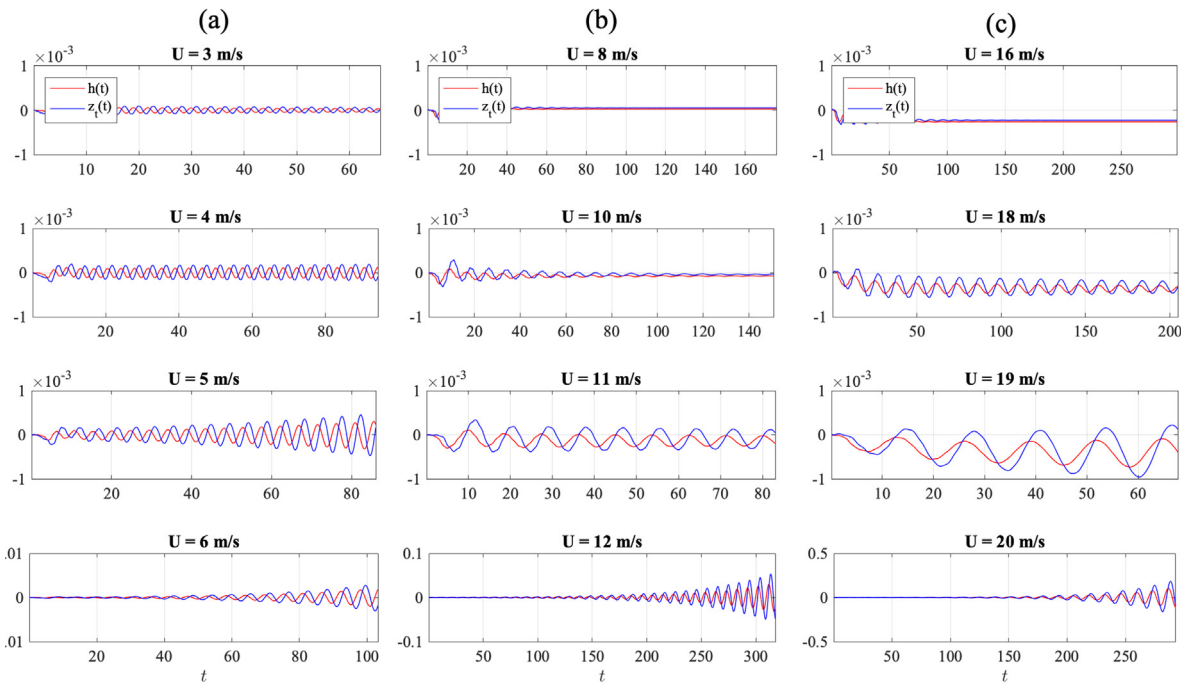

Fig. 11. Non-dimensional leading- and trailing-edge time evolutions, $h(t)$ and $z_t(t)$, for a CF plate of $c = 1$ m with $\tilde{k}_h = 100$ kg/m s^2 and $\tilde{b}_h = 0$, and three values of ε/c, arranged in three columns for increasing wind velocity U, as indicated: column (a) for $\varepsilon/c = 10^{-3}$, (b) for $\varepsilon/c = 1.5 \times 10^{-3}$, and (c) for $\varepsilon/c = 2 \times 10^{-3}$ (c). Only some initial parts of the full computations are shown.

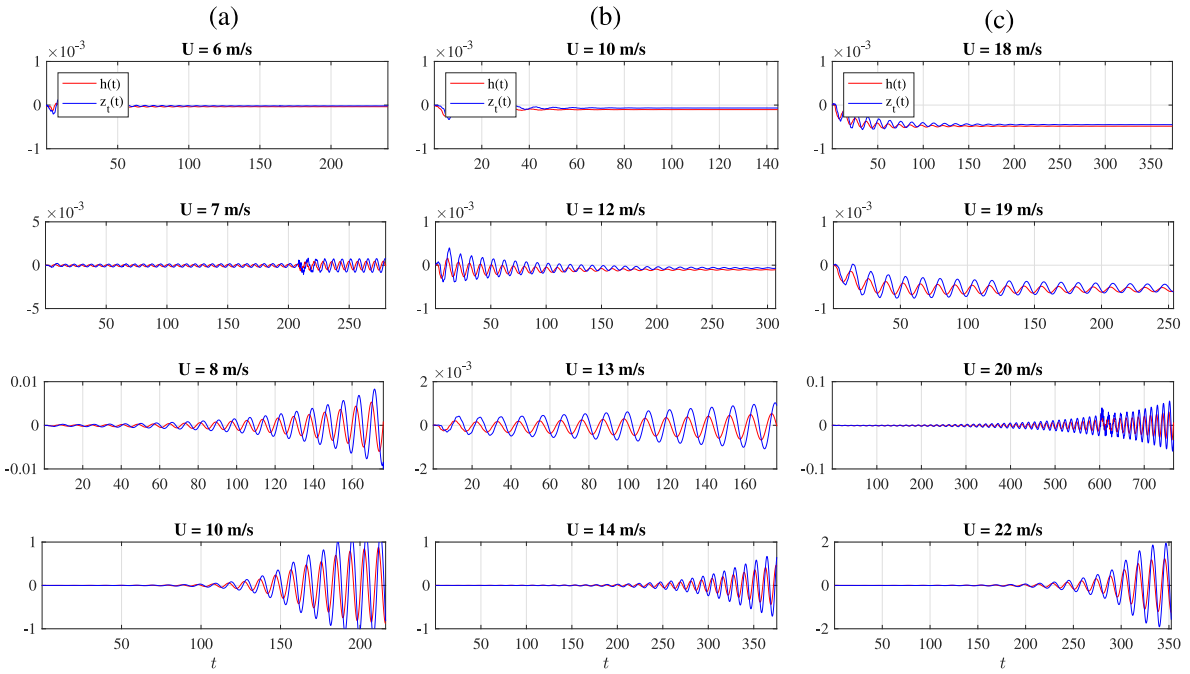

Fig. 12. As in Fig. 11, but for $\tilde{b}_h = 1$ kg/m s and $\tilde{k}_h = 75$ kg/m s^2.

$\dot{h}_{max}$ for all the unstable cases considered in Figs. 11 and 12 are reported in Tables 1 and 2, respectively. The separation of the flow on the extrados increases with both U and $\dot{h}_{max}$.

Tables 1 and 2 also contains the flutter instability frequencies computed numerically. They are in close agreement with the frequencies predicted by the theory [compare with the frequencies at the white dots marked in Figs. 5(a) and

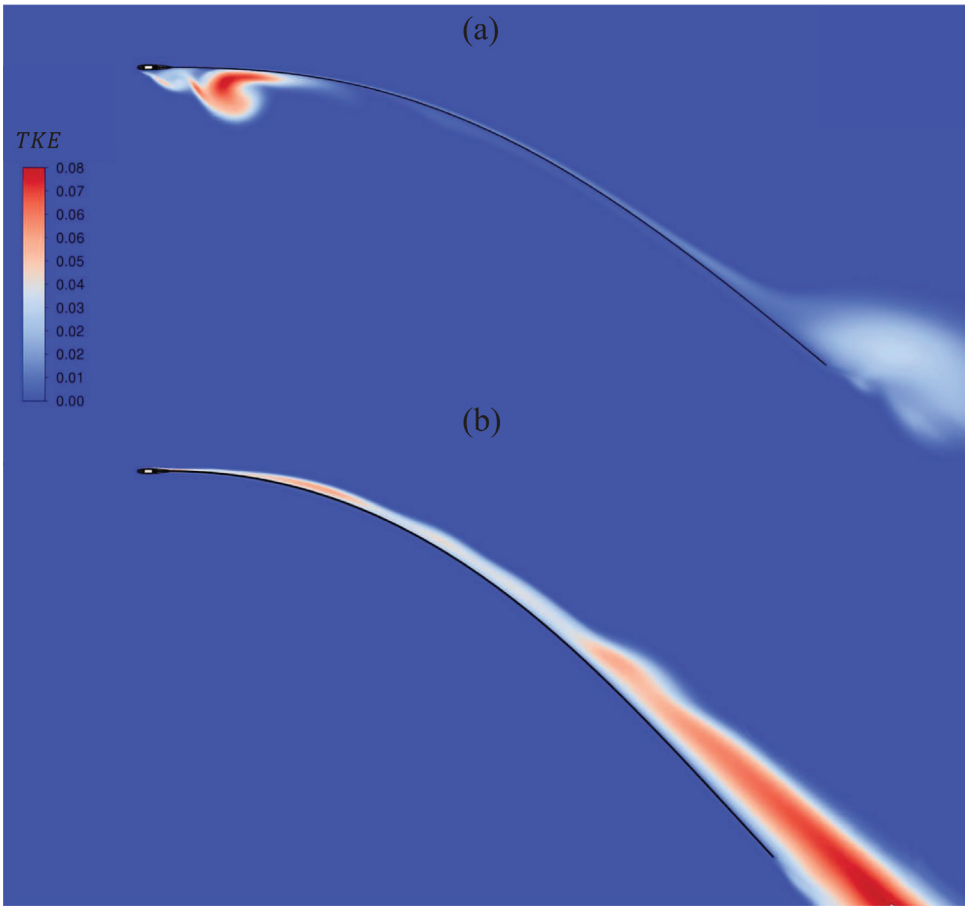

Fig. 13. Snapshots of the dimensionless turbulent kinetic energy (TKE) scaled with U^2 at the beginning of a flutter period (i.e. when $h = 0$ and the plate is going up) once the flutter oscillations have reached a permanent state for two cases shown in Fig. 12: (a) that corresponding to $\varepsilon/c = 10^{-3}$ with $U = 8$ m/s [third frame in Fig. 12(a)], and (b) corresponding to $\varepsilon/c = 2 \times 10^{-3}$ with $U = 20$ m/s [third frame in Fig. 12(c)].

Table 1
Frequencies in Hz and non-dimensional maxima of the heaving velocities for the cases plotted in Fig. 11. No data are shown for the stable cases, marked with "–".

$\tilde{k}_h = 100$ kg/ms^2, $\tilde{b}_h = 0$				
$\varepsilon/c = 10^{-3}$	$U = 3$ m/s	$U = 4$ m/s	$U = 5$ m/s	$U = 6$ m/s
f (Hz)	–	2.10	2.105	2.11
$\dot{h}_{max}$	–	2.2×10^{-4}	4.1×10^{-3}	0.05
$\varepsilon/c = 1.5 \times 10^{-3}$	$U = 8$ m/s	$U = 10$ m/s	$U = 11$ m/s	$U = 12$ m/s
f (Hz)	–	–	–	2.50
$\dot{h}_{max}$	–	–	–	0.01
$\varepsilon/c = 2 \times 10^{-3}$	$U = 16$ m/s	$U = 18$ m/s	$U = 19$ m/s	$U = 20$ m/s
f (Hz)	–	–	2.94	3.13
$\dot{h}_{max}$	–	–	0.02	0.5

6(a), respectively], even for the cases with larger plate thicknesses, when the theory underestimates the critical flutter wind velocity [except for the cases lying above the white dashed line in Figs. 5(a) and 6(b), where the foil stiffness is too low for the theory to hold]. Table 2, that corresponds to a value of the damper constant $b_h \neq 0$, also includes the values of the time-average power coefficient (20). They are relatively low due to the choice of springs and dampers, which have been selected from the theoretical formulation to minimize the critical flutter wind velocity for a given foil material and dimensions, not to optimize the output power, which necessarily must be obtained from full numerical computations. But this numerical optimization of the power output, which is out of the scope of the present work, can be guided by the analytical formulation presented in this paper, that selects the desired range of flutter wind velocities and

Table 2
Frequencies in Hz, non-dimensional maxima of the heaving velocities and time-averaged power coefficients for the cases plotted in Fig. 12. No data are shown for the stable cases, marked with "–".

$\tilde{k}_h = 75$ kg/ms^2, $\tilde{b}_h = 1$ kg/ms				
$\varepsilon/c = 10^{-3}$	$U = 6$ m/s	$U = 7$ m/s	$U = 8$ m/s	$U = 10$ m/s
f (Hz)	–	1.96	2.06	2.25
$\dot{h}_{max}$	–	0.01	0.4	0.64
$\overline{C}_P$	–	4.08×10^{-6}	0.019	0.036
$\varepsilon/c = 1.5 \times 10^{-3}$	$U = 10$ m/s	$U = 12$ m/s	$U = 13$ m/s	$U = 14$ m/s
f (Hz)	–	–	2.38	2.47
$\dot{h}_{max}$	–	–	5×10^{-3}	0.5
$\overline{C}_P$	–	–	2×10^{-8}	0.014
$\varepsilon/c = 2 \times 10^{-3}$	$U = 18$ m/s	$U = 19$ m/s	$U = 20$ m/s	$U = 22$ m/s
f (Hz)	–	–	3.13	3.23
$\dot{h}_{max}$	–	–	0.44	0.56
$\overline{C}_P$	–	–	0.0082	0.012

the corresponding frequencies by combining the different materials and dimensions of the plate with appropriate springs and dampers.

5. Conclusion

It has been shown through accurate numerical simulations that an analytical expression for the onset of flutter instability of a flexible foil elastically mounted to spring and damper at the leading edge correctly predicts the parametric range for wind energy harvesting of this simple mechanical device, especially in the lower range of critical flutter wind velocities. As the critical flutter velocity increases with, for instance, the thickness of the foil, the theory underestimates it owing to the separation of the flow, but the simple theoretical formulation accurately predicts the frequency of the foil oscillations after instability for all wind velocities within its validity range, i.e. when the stiffness of the foil is large enough. The theory cannot provide the power extracted from the wind, which must be obtained numerically. Full numerical simulations of the interaction between the wind and the very thin flexible foil are however complex and computationally expensive, demanding days or weeks of CPU in a supercomputer for each simple case. We propose here the combination of the theoretical formulation with punctual numerical simulations as a powerful tool for searching optimal conditions for energy harvesting with this flexible flapping foil device. The analysis of the present paper shows that energy can be harvested at quite low wind velocities.

We have just explored one foil material with several thickness-to-chord ratios mounted to particular springs and dampers in a range of wind velocities, comparing with full numerical simulations for a selected set of cases. But the flutter velocities can be lower and the power output larger for other materials, springs and dampers, which can conveniently be selected using the theory in a given range of wind velocities and with the desired frequency range of the flutter oscillations. For instance, the theory predicts that the minimum wind velocity for energy extraction decreases with $(E/\rho)(\varepsilon/c)^{3/2}$, where E is the elastic modulus, ρ the air density, and ε/c the thickness-to-chord ratio of the plate. The corresponding frequency is proportional to $(E/\rho_s)^{1/2}\varepsilon/c^2$, where ρ_s is the density of the foil. Thus, one may select $(E/\rho)(\varepsilon/c)^{3/2}$ for a given range of critical flutter wind speeds, ρ_s and c for the desired frequency, and then vary the spring and damper constants to optimize the energy efficiency trough full numerical simulations.

CRediT authorship contribution statement

R. Fernandez-Feria: Conceptualization, Data curation, Formal analysis, Funding acquisition, Investigation, Methodology, Resources, Software, Supervision, Validation, Visualization, Writing – original draft, Writing – review & editing. **E. Sanmiguel-Rojas:** Conceptualization, Data curation, Funding acquisition, Investigation, Methodology, Project administration, Resources, Software, Supervision, Validation, Visualization, Writing – review & editing.

Declaration of competing interest

The authors declare that they have no known competing financial interests or personal relationships that could have appeared to influence the work reported in this paper.

Data availability

Data will be made available on request.

Acknowledgments

This research has been financed by the *Ministerio de Ciencia e Innovación* of Spain (PID2019-104938RB-I00). The computations were performed in the Picasso Supercomputer at the University of Málaga, a node of the Spanish Supercomputing Network. Funding for open access charge: Universidad de Málaga / CBUA.

Appendix. Coefficients in Eq. (10)

These coefficients are

$$A_{11} = -m\gamma^2 + k_h + b_h i\gamma + A_{11}^F\,, \tag{A.1}$$

$$A_{12} = -J_a\gamma^2 + A_{12}^F\,, \tag{A.2}$$

$$A_{21} = -I_a\gamma^2 + A_{21}^F\,, \tag{A.3}$$

$$A_{22} = -K_d\gamma^2 + \frac{16}{9}S + A_{33}^F\,, \tag{A.4}$$

where the superscript F refers to the contributions to these coefficients from the fluid–structure interaction (i.e., from C_L, and C_F). Using the expressions of C_L and C_F (see Fernandez-Feria, 2022, in absence of pitching motion and with $a = 1$), these contributions can be written as

$$A_{11}^F = \pi\gamma[-\gamma + 2i\mathcal{C}(\gamma)]\,, \tag{A.5}$$

$$A_{12}^F = \pi\left[-\frac{149}{192}\gamma^2 + \frac{25}{24}i\gamma + \mathcal{C}(\gamma)\left(\frac{263}{96}i\gamma + \frac{59}{24}\right)\right], \tag{A.6}$$

$$A_{21}^F = \pi\left[-\frac{5}{4}\gamma^2 + \mathcal{C}(\gamma)i\gamma\right], \tag{A.7}$$

$$A_{22}^F = \pi\left[-\frac{1915}{1536}\gamma^2 + \frac{113}{48}i\gamma + \frac{11}{48} + \mathcal{C}(\gamma)\left(\frac{263}{192}i\gamma + \frac{59}{48}\right)\right], \tag{A.8}$$

where $\mathcal{C}(\gamma)$ is Theothorsen's function of the complex argument γ.

References

Abiru, H., Yoshitake, A., 2011. Study on a flapping wing hydroelectric power generation system. J. Environ. Eng. 6 (178).
Alben, S., 2008. Optimal flexibility of a flapping appendage in an inviscid fluid. J. Fluid Mech. 614, 355–380.
Allen, J.J., Smits, A.J., 2001. Energy harvesting eel. J. Fluids Struct. 15, 629–640.
Boudreau, M., Dumas, G., Rahimpour, M., Oshkai, P., 2018. Experimental investigation of the energy extraction by a fully-passive flapping-foil hydrokinetic turbine prototype. J. Fluids Struct. 82, 446–472.
Boudreau, M., Gunther, K., Dumas, G., 2019a. Free-pitching flapping-foil turbines with imposed sinusoidal heave. J. Fluids Struct. 90, 110–138.
Boudreau, M., Gunther, K., Dumas, G., 2019b. Investigation of the energy-extraction regime of a novel semi-passive flapping-foil turbine concept with a prescribed heave motion and a passive pitch motion. J. Fluids Struct. 84, 368–390.
Boudreau, M., Picard-Deland, M., Dumas, G., 2020. A parametric study and optimization of the fully-passive flapping-foil turbine at high Reynolds number. Renew. Energy 146, 1958–1975.
Deng, J., Caulfield, C.P., Shao, X., 2014. Effect of aspect ratio on the energy extraction efficiency of three-dimensional flapping foils. Phys. Fluids 26, 043102.
Eloy, C., Lagrange, R., Souilliez, C., Schouveiler, L., 2008. Aeroelastic instability of a flexible plate in a uniform flow. J. Fluid Mech. 611, 97–106.
Fernandez-Feria, 2022. Flutter stability analysis of an elastically supported flexible foil, application to the energy harvesting of a fully-passive flexible flapping-foil of small amplitude. J. Fluids Struct. 109, 103454.
Fernandez-Feria, R., Alaminos-Quesada, J., 2021. Analytical results for the propulsion performance of a flexible foil with prescribed pitching and heaving motions and passive small deflection. J. Fluid Mech. 910, A43.
Gharali, K., Johnson, D.A., 2013. Dynamic stall simulation of a pitching airfoil under unsteady freestream velocity. J. Fluids Struct. 42, 228–244.
Hamlehdar, M., Kasaeian, A., Safaei, M.R., 2019. Energy harvesting from fluid flow using piezoelectrics: A critical review. Renew. Energy 143, 1826–1838.
Heathcote, S., Gursul, I., 2007. Flexible flapping airfoil propulsion at low Reynolds numbers. AIAA J. 45, 1066–1079.
Jeanmonod, G., Olivier, M., 2017. Effects of chordwise flexibility on 2D flapping foils used as an energy extraction device. J. Fluids Struct. 70, 327–345.
Khaligh, A., Zeng, P., Zheng, C., 2010. Kinetic energy harvesting using piezoelectric and electromagnetic technologies - State of the art. IEEE Trans. Ind. Electron. 57, 850–860.

Kim, D., Strom, B., Mandre, S., Breuer, K., 2017. Energy harvesting performance and flow structure of an oscillating hydrofoil with finite span. J. Fluids Struct. 70, 314–326.
Kinsey, T., Dumas, G., 2008. Parametric study of an oscillating airfoil in a power-extraction regime. AIAA J. 46 (6), 1318–1330.
Lee, Y.J., Qi, Y., Zhou, G., Lua, K.B., 2019. Vortex-induced vibration wind energy harvesting by piezoelectric mems device in formation. Sci. Rep. 9, 20404.
Liu, Z., Tian, F.B., Young, J., Lai, J.C.S., 2017. Flapping foil power generator performance enhanced with a spring-connected tail. Phys. Fluids 29 (12), 123601.
Liu, W., Xiao, Q., Cheng, F., 2013. A bio-inspired study on tidal energy extraction with flexible flapping wings. Bioinspiration Biomim. 8 (3), 036011.
Liu, W., Xiao, Q., Zhu, Q., 2016. Passive flexibility effect on oscillating foil energy harvester. AIAA J. 54 (4), 1172–1187.
McKenna, R., Pfenninger, S., Heinrichs, H., Schmidt, J., Staffell, I., Bauer, C., Gruber, K., Nahmann, A.N., et al., 2022. High-resolution large-scale onshore wind energy assessments: A review of potential definitions, methodologies and future research needs. Renew. Energy 182, 659–684.
McKinney, W., DeLaurier, J., 1981. Wingmill: An oscillating-wing windmill. AIAA J. Energy 5 (2), 109.
Michelin, S., Llewellyn Smith, S.G., Glover, B.J., 2008. Vortex shedding model of a flapping flag. J. Fluid Mech. 617, 1–10.
Newmark, N.M., 1959. A method of computation for structural dynamics. J. Eng. Mec, ASCE 85, 67–94.
Peng, Z., Zhu, Q., 2009. Energy harvesting through flow-induced oscillations on a foil. Phys. Fluids 21, 123602.
Quang, L.T., Hwan, K.J., 2015. Effect of hydrofoil flexibility on the power extraction of a flapping tidal generator via two- and three-dimensional flow simulations. Renew. Energy 80, 275–285.
Sanmiguel-Rojas, E., Fernandez-Feria, R., 2021. Propulsion enhancement of flexible plunging foils: Comparing linear theory predictions with high-fidelity CFD results. Ocean Eng. 235, 109331.
Sanmiguel-Rojas, E., Fernandez-Feria, R., 2022. Numerical study of the propulsive performance of two-dimensional pitching foils at very high frequencies: Scaling laws and turbulence effects. Int. J. Numer. Methods Heat Fluid Flow 32 (5), 1602–1617.
Shelley, M., Vandenberghe, N., Zhang, J., 2005. Heavy flags undergo spontaneous oscillations in flowing water. Phys. Rev. Lett. 94, 094302.
Shimizu, E., Isogai, K., Obayashi, S., 2008. Multiobjective design study of a flapping wing power generator. J. Fluids Eng. 130, 021104.
Su, Y., Breuer, K., 2019. Resonant response and optimal energy harvesting of an elastically mounted pitching and heaving hydrofoil. Phys. Rev. Fluids 4, 064701.
Tamimi, V., Wu, J., Esfehani, M.J., Zeinoddini, M., Naeeni, S.T.O., 2022. Comparison of hydrokinetic energy harvesting performance of a fluttering hydrofoil against other flow-induced vibration (FIV) mechanisms. Renew. Energy 186, 157–172.
Tang, L., Païdoussis, M.P., 2007. On the instability and the post-critical behaviour of two-dimensional cantilevered flexible plates in axial flow. J. Sound Vib. 305, 97–115.
Tang, L., Païdoussis, M.P., Jiang, J., 2009. Cantilevered flexible plates in axial flow: Energy transfer and the concept of flutter-mill. J. Sound Vib. 326, 263–276.
Veilleux, J.C., Dumas, G., 2017. Numerical optimization of a fully-passive flapping-airfoil turbine. J. Fluids Struct. 70, 102–130.
Wang, Z., Du, L., Zhao, J., Sun, X., 2017. Structural response and energy extraction of a fully passive flapping foil. J. Fluids Struct. 72, 96–113.
Wu, J., Shu, C., Zhao, N., Tian, F.B., 2015. Numerical study on the power extraction performance of a flapping foil with a flexible tail. Phys. Fluids 27, 013602.
Xiao, Q., Zhu, Q., 2014. A review on flow energy harvesting based on flapping foils. J. Fluids Struct. 46, 174–191.
Young, J., Lai, J.C.S., Platzer, M.F., 2014. A review of progress and challenges in flapping foil power generation. Prog. Aerosp. Sci. 67, 2–28.
Zhu, Q., 2012. Energy harvesting by a purely passive flapping foil from shear flows. J. Fluids Struct. 34, 157–169.
Zhu, Q., Haase, M., Wu, C.H., 2009. Modeling the capacity of a novel flow-energy harvester. Appl. Math. Model 130, 2207–2217.
Zhu, Q., Peng, Z., 2009. Mode coupling and flow energy harvesting by a flapping foil. Phys. Fluids 21, 033601.
Zhu, B., Xia, P., Huang, Y., Zhang, W., 2019. Energy extraction properties of a flapping wing with an arc-deformable airfoil. J. Renew. Sustain. Energy 11, 023302.